Laser-processing with colloid monolayers

Dieter Bäuerle*[a], Lars Landström[b], Johannes Kofler[a], Nikita Arnold[a], Klaus Piglmayer[a]

[a] Angewandte Physik, Johannes-Kepler-Universität, Altenbergerstraße 69,
A-4040, Linz, Austria

[b] On leave from The Ångström Laboratory, Dept. of Materials Chemistry,
Uppsala University, Box 538, SE-75121 Uppsala, Sweden

ABSTRACT

Two-dimensional (2D) lattices of microspheres formed by self-assembly from colloidal solutions have been used for laser-induced surface patterning by ablation, etching, deposition, and surface modification. The imageing properties of microspheres and the related intensity- and temperature-distributions on nearby substrates are studied and compared with experimental results on the deposition of Pd from aqueous solutions of $PdCl_2$ in NH_3 .

Keywords: Laser processing, surface patterning, optical properties of microspheres, liquid-phase deposition.

1. INTRODUCTION

Different types of laser-induced surface patterning, coating, and physico-chemical modification have been reviewed in Ref. 1. Laser-induced micro- and submicro-patterning has been demonstrated by direct focussing of the laser light onto the substrate (direct writing), by projecting it via a mechanical mask, by employing a contact mask, or by laser-beam interference. At present, we are investigating a new technique for single-step surface patterning. Here, we employ regular two-dimensional (2D) lattices of microspheres which are formed by well-known self-assembly processes, e.g. from colloidal suspensions. In contrast to earlier investigations we use such 2D lattices not as masks for consecutive processing[2,3], but as an array of microlenses on a transparent support. Thus, the microspheres are used to focus the incident laser radiation onto the substrate, albeit with significant (spherical) aberration. The technique permits one to produce on a substrate surface thousands or millions of single submicron features with a single or a few laser shots[4-9]. By using such a 2D lattice of microspheres, single-shot KrF-laser radiation and a fused quartz support with a monolayer of a-SiO_2 spheres of various diameters, we have generated 2D ablation patterns on polymers such as polyethyleneterephthalate (PET)[5] and polyimide (PI)[6]. In a similar way we have demonstrated the growth of circular cones on (100) Si wafers[8]. Surface patterning of thin W films on a-SiO_2 substrates by reactive etching in WF_6 atmosphere under 514.5 nm Ar^+-laser radiation has been investigated in Ref. 9. Similarly, the deposition of arrays of W dots has been demonstrated by using a mixture of WF_6 and H_2[9].

2. IMAGEING PROPERTIES OF MICROSPHERES

According to geometrical optics, the focus of a sphere with radius $r \gg \lambda$ and refractive index n is given by

$$f = \frac{r}{2}\frac{n*}{n*-1} \qquad (1)$$

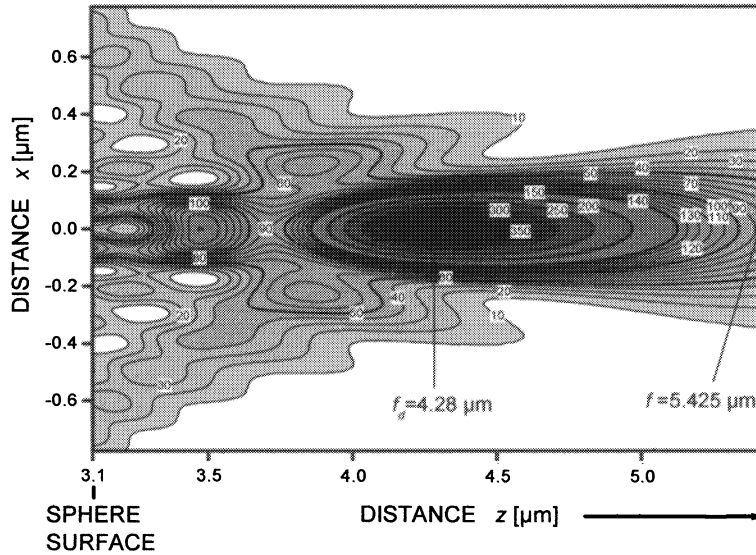* dieter.baeuerle@jku.at; phone ++43 732 2468 9243; fax ++43 732 2468 9242

Fig. 1. Normalized intensity distribution $I/I_o \equiv |E(x,z)|^2 / |E_O|^2$ behind a particle of radius $r=3.1$ μm with $n = 1.4$ calculated on the basis of the Mie theory with $kr =79$. The incident 248 nm KrF-laser radiation with intensity $|E_O|^2$ is polarized in x-direction. z is the distance from the center of the microsphere. The position f_d calculated from eq. (2) is also indicated.
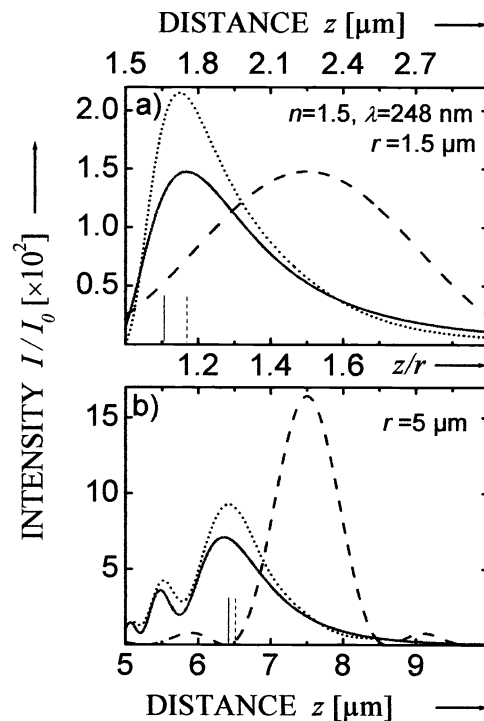

Fig. 2. Normalized intensity distributions for microspheres calculated as a function of distance z for $\lambda = 248$ nm radiation and $n = 1.5$. Solid curves are calculated from eq. (3). Dotted curves are exact Mie results (same as in Fig. 1 for $x = 0$). Dashed curves are obtained from the aberrationless expressions given in [11] for an aperture $a = r$. The thin solid and dashed lines show the positions of f_d calculated from (2) and from the condition $\varphi_{np} - \varphi_p = \pi/2$, respectively.

where f is measured from the center of the sphere and $n* = n / n_a$. Here, n_a is the refractive index of the ambient medium. In reality, *spherical aberration* shifts the diffraction focus towards the sphere and results in a complex intensity distribution which can be calculated only numerically. Figure 1 shows the normalized intensity distribution $I / I_o \equiv |E(x,z)|^2 / |E_0|^2$ calculated on the basis of the Mie theory. Here, $E(x,z)$ is the electric field behind the sphere for an incident plane wave propagating in z-direction and polarized in x-direction. It is calculated for a sphere of radius $r = 3.1$ µm and refractive indices $n = 1.4$ and $n_a = 1$. For these parameter values we obtain from (1) a focal length $f \approx 5.4$ µm. The figure shows that the maximum intensity occurs at a distance much smaller than f. The highest intensity occurs along the symmetry axis within a small caustic radius $w_c \approx C(z) \lambda$ where $C(z = r) \approx 0.2$. According to geometrical optics, the width of the distribution in the plane $z = r$ is, approximately, given by $w_g \approx r(4 - n*^2)^{3/2} / 3\sqrt{3} \ n*^2$. An interesting feature occurs near the center $x \approx 0$. Here, a double maximum which is oriented along the polarization of the incoming light is observed. Such a "dipolar" intensity distribution is well known for particles that are much smaller than the wavelength, i.e. when $r \ll \lambda$. In such cases it can be understood from the interference of the near-field dipole field with the incoming light. However, in the present case with $r \gg \lambda$, the enhancement is orders of magnitude higher.

The position of the diffraction focus, f_d, defined by the maximum intensity, can be found as follows. The intensity on the axis is essentially determined by the interference between the cone of *non-paraxial* sagittal rays with the same phase φ_{np}, and a single *paraxial* ray of phase φ_p. These phases can be calculated in the approximation of geometrical optics. Constructive interference is obtained if $(\varphi_{np} - \pi / 2) - \varphi_p = 0, \pm 2\pi, \pm 4\pi...$. This explains qualitatively the oscillating intensity along the z-axis. The term $\pi/2$ takes into account the caustic phase shift of all non-paraxial rays[10]. In the lowest order of the Mie parameter kr and in the case that all the angles are small, we obtain

$$f_d = \frac{r}{2} \frac{n}{n - n_a} \left(1 - \sqrt{\frac{\pi}{2} \ \frac{n \ (3n_a - n) - n_a}{n(n - n_a)n_a \ kr}} \ \right) \qquad (2)$$

This expression illustrates the influence of the *size* of spheres on the relative focal position. In contrast to the case of weak aberration[11], the ratio f_d / f depends on kr. Mie calculations also do *not* provide an explicit analytical expression for f_d.

In order to obtain further insight into the imageing properties of microspheres, we calculate the field along the z-axis for $z \geq r$ by adding up contributions from virtual point sources in the plane $z = -r$. Single rays from these sources are incident at a certain point of observation with different angles θ and phases φ. This approach is similar to that of a standard Kirchhoff integral. The distance from the point sources, R, in the denominator of this integral is replaced by $\sqrt{R_1 R_2}$, where $R_{1,2}$ are the principal radii of curvature of virtual wavefronts[10]. We consider only rays with two refractions at the sphere surface. The vector nature of the electromagnetic field is included via the Fresnel reflection and transmission coefficients. The field from the areas not shadowed by the sphere is neglected. After Taylor expansion in θ, the field along the z-axis can be described by

$$E(z) \approx E_0 \exp[i\psi_0] \int_0^{\xi_m} (g_0 + g_1\xi) \exp[i(\psi_1\xi + \psi_2\xi^2)] \, d\xi. \qquad (3)$$

where $\xi = \theta^2/2$. The coefficients ψ_i and g_i depend on z, r, $n*$ and $k = 2\pi/\lambda$. At $z = f$ we have $\psi_1 = 0$. ψ_2 describes the spherical aberration. The details of the calculations and expressions for these coefficients will be presented elsewhere. The integral can be expressed via Fresnel integrals or calculated in the stationary-phase approximation.

Stationary phase analysis shows that the leading term in the intensity is $I(z) \propto k \ r$ with I_{max} at $z = f_d$. This is indeed typical for strong spherical aberration. It has been outlined in Ref.10 that in this case $I \propto f / \lambda$. With (1) we find $I \propto k \ r$.

This term *alone* yields a reasonable approximation for $kr > 500$. For an equivalent *aberrationless* lens we find $I_{max} \propto (kr)^2$ in the focal point f, and a depth of focus of about λ.

The solid curves in Fig. 2 show the normalized intensities along the z-axis, calculated from (3) for two different sizes of microspheres. These are compared with the intensities obtained from the Mie theory (dotted curves) and from aberrationless expressions (dashed curves). In particular for larger spheres, the exact Mie results are well reproduced by the diffraction approximation. Thus, it is elucidating to consider Mie scattering near the sphere as a diffraction pattern of a focused aberrated wave. The figures clearly show that strong spherical aberration significantly decreases the focal intensity, but creates a high intensity line between the sphere and the focus.

Both equation (3) and the simple approximation (2), reflect a pronounced shift of the diffraction focus towards the surface of the sphere as compared to geometrical optics. For even smaller spheres, the maximum of the intensity is reached at the surface and may contain strong near-field contributions[13].

3. COMPARISON WITH EXPERIMENTAL RESULTS

The intensity distribution depicted in Fig. 1 can qualitatively explain some of the peculiarities observed in a number of processing applications. For example, in connection with dry-laser cleaning local field enhancements below spherical particulates result in local substrate damage and, in many cases, in local laser-induced ablation of the substrate material[14,15]. The "dipolar" intensity distribution in the plane $z \approx r$ has been recently observed via a double hole structure obtained during ablation of 1 µm Ni foils by means of 500 fs KrF-laser pulses[4]. In this case, the 6.6 µm microspheres employed in the experiments were in close contact to the metal foil. Another feature refers to the aspect ratio of holes generated by means of 2D lattices of microspheres by laser ablation[4-7]. The high aspect ratios achieved in these experiments may be related to the line-type focus shown in Fig. 1. Such a line-type focus avoids rapid changes in the local laser-induced intensity with increasing depth of holes. The figure also suggests that in processing cases where high spatial resolution is desired, substrate positioning closer than f_d may be preferred. With pyrolytic processes, however, one has to keep in mind that the laser-induced temperature distribution will depend in a non-trivial way on the laser-light intensity and pulse duration.

In the following we will apply the picture developed in Sect. 2 for the analysis of Pd dots deposited from liquid-phase precursors.

4. LIQUID-PHASE DEPOSITION

Laser processing by means of liquid-phase instead of gas-phase precursors permits higher reaction rates and avoids problems of reactant depletion related to the narrow gap between the spheres and the substrate. According to (1) and (2), the higher index of refraction of the liquid, compared to a gas, leads to a longer focal distance. This results in both a smaller influence of the working distance on the experimental results and a higher amount of precursor molecules available for the local reaction.

4.1 Deposition of Palladium
Palladium has been deposited from a solution of 0.1 mol $PdCl_2$ in 1 mol aqueous NH_3. With this mixture, stable amine-complexes are formed, the majority being palladium-tetra-amine $Pd(NH_3)_4^{2+}$. The final solution has a pH of about 11.5 (Ref. 16).

Experiments were performed at a distance of $z \approx 20.8$ µm and 8.8 µm. The first value corresponds approximately to the diffractive focal length of a microsphere within the liquid precursor. All deposits reflect the hexagonally close-packed structure of the microspheres characterized by the average distance $d = 2r = 6.6$ µm. The deposits were characterized by means of optical microscopy, atomic force microscopy (AFM) and X-ray photoelectron spectroscopy (XPS).

Pd patterns were deposited by means of both 248 nm KrF- and 350 nm Ar$^+$-laser radiation. The substrate materials were PI foils and mica[17]. The dots deposited by means of 248 nm radiation are large-grain polycrystalline with a diameter of 3.6 ± 0.5 μm. First results have been reported in Ref. 4. The dots deposited with 350 nm radiation have a fine-grain morphology and are much smoother. Figure 3 shows an optical microscope picture of such dots. A typical thickness profile is shown in Fig. 4a.

An XPS analysis of both KrF- and Ar$^+$-laser deposited dots reveals that the deposits consist in both cases mainly of Pd. This was confirmed from the relative intensities and locations of the Pd $3d_{5/2}$ and Pd $3d_{3/2}$ peaks, at 335 and 340 eV, respectively. In order to get more insight into the deposition mechanisms, we estimate the intensity- and temperature-distributions behind the 2D lattice of microspheres.

4.2 Intensity- and temperature-distributions

Because the refractive indices of the silica spheres and the ambient aqueous solution are rather close, the focal distance becomes pretty large. From (1) and (2) we find $f \approx 42$ μm and $f_d \approx 13$ μm, respectively. These values are quite inaccurate because n and n_a are also not exactly known. From numerical calculations of geometrical phase differences with the condition $(\varphi_{np} - \pi/2) = \varphi_p$ we find $f_d \approx 21$ μm. This value is in good agreement with Mie calculations which yield $f_d \approx 22$ μm. Because it is unclear whether the deposition of Pd is based on a mainly pyrolytic or mainly photolytic decomposition process, we have calculated both the intensity distribution and the thermal reaction rate. The intensity defined as the z-component of the Poynting vector, S_z, was calculated from the Mie formulas. This flux, normalized to the intensity of the incident plane wave polarized in x-direction, is shown in Fig. 4b by the dotted curve. The effective Mie parameter was $n_a kr = 80$. The temperature distribution was calculated by assuming surface absorption within the deposit and no lateral heat conduction in the deposit. Taking into account the measured thicknesses of Pd deposits, this latter assumption is certainly a very crude approximation. Henceforth, we also ignore convection within the liquid. Finally, with the laser pulse length employed, $\tau_\ell = 10$ ms, we can assume stationary conditions. With these assumptions, the linearized temperature rise at the interface between the liquid and the substrate is given by
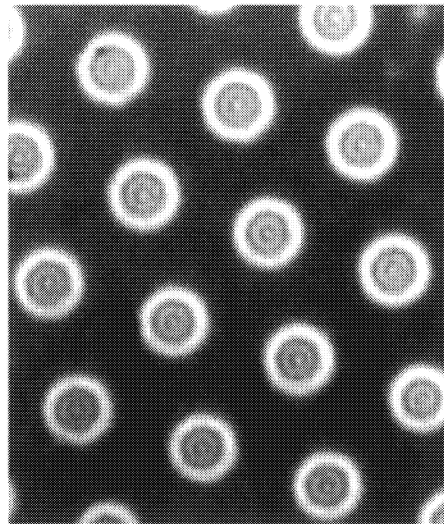

Fig. 3: Optical microscope picture of Pd dots deposited from an aqueous solution of 0.1 mol PdCl$_2$ in 1 mol NH$_3$ using a-SiO$_2$ microspheres of diameter $d = 6.6$ μm, 350 nm Ar$^+$-laser radiation ($\phi = 25$ J/cm^2, $\tau_\ell = 10$ ms, $N_\ell = 90$) and $z = 8.8$ μm. The substrate was PI.
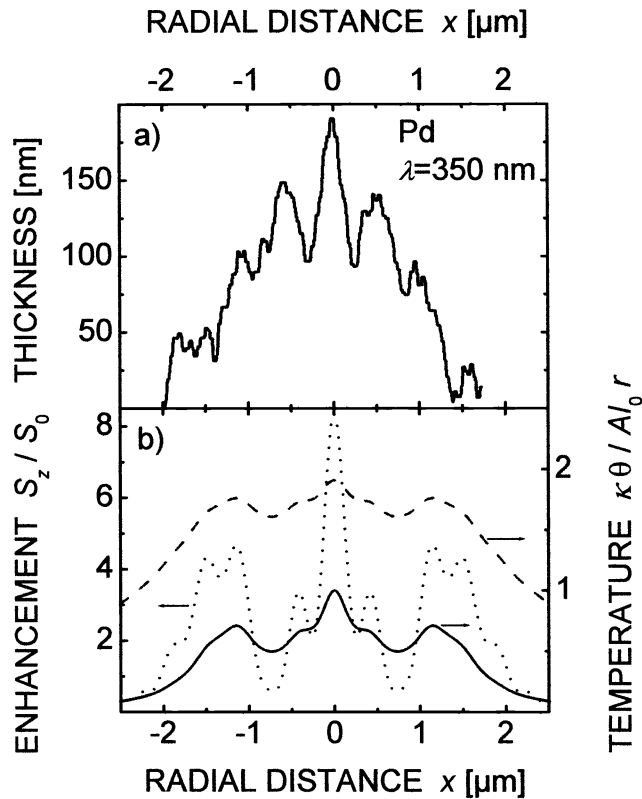
RADIAL DISTANCE x [μm]

Fig. 4: a) Typical thickness profile of a Pd deposit shown in Fig. 3. b) Calculated profiles of the normalized intensity flux (dotted curve), temperature distribution (dashed curve), and thermal reaction rate for 350 nm Ar⁺-laser radiation (full curve). The other parameters were $d = 6.6$ μm, $n = 1.4$, $n_a = 1.345$, and $z = 8.8$ μm.

$$\theta(x) = \frac{2}{\pi} \frac{AI_0}{\kappa} \int_0^\infty dx_1 S(x_1) \left. \begin{cases} (x_1/x)K(x_1^2/x^2) \\ K(x^2/x_1^2) \end{cases} \right\} \begin{array}{l} with \quad x_1 < x \\ " \quad\quad x_1 > x \end{array} \tag{4}$$

where A is the absorptivity and κ the thermal conductivity. The latter includes fluxes into both the substrate and the liquid, i.e. $\kappa = \kappa_s + \kappa_l$. The function S is the (dimensionless) intensity enhancement due to the focusing of the radiation by the microspheres. In the present analysis, $S(x)$ is taken from the Mie calculations. K is the complete elliptic integral of the first kind. The 1D integral was obtained by assuming an axially symmetric intensity distribution. The dimensionless temperature rise, $\theta\kappa / AI_0 r$ which is numerically calculated from (4) is included in Fig. 4b by the dashed curve. With $A = 1$, $\kappa = 0.07$ W/cmK, $I_0 = 2546$ W/cm² and $r = 3.3$ μm one unit corresponds to 12 K. The background heating over $N_\ell = 90$ pulses with the pulse duration $\tau_\ell = 10$ ms, $\nu_\ell = 1$ Hz repetition rate (average intensity $<I_0> \equiv \nu_\ell \tau I_0 = 25.5$ W/cm²) can be estimated from $\Delta T \approx (A < I_0 > w/\sqrt{\pi}\kappa) \arctan(2\sqrt{Dt}/w)$. With a heat diffusivity $D = 0.015$ cm²/s, a spot size of the incident laser beam $w = 50$ μm and a total irradiation time $t = N_\ell/\nu_\ell = 90$ s we obtain $\Delta T \approx 1.6$ K. The full curve in Fig. 4b shows the normalized reaction rate for a background temperature $T_o = 300$ K and an activation temperature $T_a \equiv \Delta E/k_B = 2\cdot 10^4$ K. The small variation of the temperature obtained in these estimations suggests that, under the conditions employed, the deposition of Pd is mainly based on a photolytic process. The broadening of features may be related to diffusion effects.

In summary we can say that investigations on the imaging properties of microspheres permit to understand qualitatively or even semiquantitatively some of the features recently observed in laser surface patterning by means of colloid monolayers.

5. ACKNOWLEDGEMENTS

REFERENCES

1. D. Bäuerle, *Laser Processing and Chemistry,* 3rd ed., Springer, Berlin, Heidelberg, 2000.
2. F. Burmeister, W. Badowsky, T. Braun, S. Wieprich, J. Boneberg, and P. Leiderer: Appl. Surf. Sci., **144-145,** 461(1999).
3. J.C. Hulteen and R.P. Van Duyne, J. Vac. Sci. Technol. A **13,** 1553 (1995).
4. D. Bäuerle, G. Wysocki, L. Landström, J. Klimstein, K. Piglmayer, and J. Heitz, "Laser-induced single step micro/nanopatterning", Proc. SPIE **5063,** 8-12 (2003)
5. R. Denk, K. Piglmayer, and D. Bäuerle, "Laser-induced nanopatterning of PET using a-SiO$_2$ microspheres". Appl. Phys. A **74,** 825-826 (2002).
6. K. Piglmayer, R. Denk, and D. Bäuerle, "Laser-induced surface patterning by means of microspheres", Appl. Phys. Lett., **80** 4693-4695 (2002).
7. R. Denk, K. Piglmayer, and D. Bäuerle, "Laser-induced nano-patterning by means of interference subpatterns generated by microspheres" Appl. Phys. A **76,** 1-3 (2003).
8. G. Wysocki, R. Denk, K. Piglmayer, N. Arnold, and D. Bäuerle, "Single-step fabrication of silicon-cone arrays" Appl. Phys. Lett. **82,** 692-692 (2003).
9. R. Denk, K. Piglmayer, and D. Bäuerle, "Laser-induced etching and deposition of W using a-SiO$_2$ microspheres" Appl. Phys. A **76,** 549-550 (2003).
10. Y. A. Kravtsov, Y. I. Orlov, *Caustics, catastrophes and wave fields,* 2nd ed., Springer, Berlin 1998; Y. A. Kravtsov, Y. I. Orlov, *Geometrical Optics of Inhomogeneous Media,* Springer, Berlin, 1990
11. M. Born and E. Wolf, *Principles of Optics,* 6th ed., Pergamon press, New York, 1980.
12. P. W. Barber and S.C. Hill, *Light scattering by particles: Computational methods,* World Scientific, Singapore, 1990.
13. B.S. Luk'yanchuk, Y.W. Zheng, and Y.F. Lu, Proc. SPIE **4065,** 576 (2000)
14. H.-J. Münzer, M. Mosbacher, M. Bertsch, O. Dubbers, A. Pack, R. Wannemacher, B.-U. Runge, D. Bäuerle, and P. Leiderer, "Optical near field effects in surface nanostructuring and laser cleaning" Proc. SPIE **4426,** 180-183 (2002)
15. N. Arnold, G. Schrems, and D. Bäuerle, "Ablative thresholds in laser cleaning of substrates from particulates", Appl. Phys. A (2004)
16. A. Narayan, L. Landström, and M. Boman, Appl. Surf. Sci. **208-209,** 137 (2003).
17. L. Landström, K. Piglmayer, D. Bäuerle, to be published